IEEE Access
Multidisciplinary | Rapid Review | Open Access Journal

Received November 30, 2020, accepted December 14, 2020, date of publication January 5, 2021, date of current version January 14, 2021.

Digital Object Identifier 10.1109/ACCESS.2021.3049451

Global Comparison of F2-Layer Peak Parameters Estimated by IRI-2016 With Ionospheric Radio Occultation Data During Solar Minimum

WEIHUA BAI[1,2,3,4,5], GUANGYUAN TAN[1,2,4,5], YUEQIANG SUN[1,2,3,4,5], JUNMING XIA[1,2,4,5], QIFEI DU[1,2,4,5], GUANGLIN YANG[1,6,7], XIANGGUANG MENG[1,2,4,5], DANYANG ZHAO[1,2,4,5], CONGLIANG LIU[1,2,4,5], YUERONG CAI[1,2,4,5], DONGWEI WANG[1,2,4,5], CONG YIN[1,2,4,5], AND PENG HU[1,2,4,5]

[1]National Space Science Center, Chinese Academy of Sciences (NSSC/CAS), Beijing 100190, China
[2]Beijing Key Laboratory of Space Environment Exploration, Chinese Academy of Sciences, Beijing 100190, China
[3]School of Astronomy and Space Science, University of Chinese Academy of Sciences, Beijing 100049, China
[4]National Space Science Center, Joint Laboratory on Occultations for Atmosphere and Climate (JLOAC), Chinese Academy of Sciences (NSSC/CAS), Beijing 100190, China
[5]Key Laboratory of Science and Technology on Space Environment Situational Awareness, Chinese Academy of Sciences (CAS), Beijing 100190, China
[6]National Meteorological Center, Chinese Meteorological Administration, Beijing 100081, China
[7]National Satellite Meteorological Center, Chinese Meteorological Administration, Beijing 100081, China

Corresponding author: Guangyuan Tan (tanguangyuan16@mails.ucas.ac.cn)

This work was supported in part by the National Natural Science Foundation of China under Grant 41405039, Grant 41775034, Grant 41405040, Grant 41505016, Grant 41505030, Grant 41606206, and Grant 42074042; in part by the Scientific Research Project of the Chinese Academy of Sciences under Grant YZ201129; and in part by the Feng Yun 3 (FY-3) Global Navigation Satellite System Occultation Sounder (GNOS) Development and Manufacture Project led by the National Space Science Center, Chinese Academy of Sciences (NSSC/CAS).

ABSTRACT The F2-layer peak parameters of the International Reference Ionosphere (IRI) model are critical to its subsequent applications because of the vital role of the peak parameters in determining other IRI model outputs. Therefore, we analyzed the statistical deviation and ionospheric climatology of NmF2/hmF2 between the most current version of the IRI model, namely IRI-2016, and ionospheric radio occultation (IRO) data, including Constellation Observing System for Meteorology Ionosphere and Climate (COSMIC) and FengYun-3C (FY3C), during the recent solar minimum in 2017–2019. The International Union of Radio Science (URSI) model for F2-layer peak electron density (NmF2) and the Bilitza–Sheikh–Eyfrig (BSE), Altadill-Magdaleno–Torta–Blanch (AMTB), and SHUbin (SHU) models for maximum ionization height (hmF2) in IRI-2016 are compared with the IRO dataset. A statistical analysis shows a systematic offset of less than 10% in NmF2 between IRI-2016 URSI and IRO data, and the SHU option for hmF2 shows a better fit to IRO data than BSE and AMTB. A climatology comparison shows that NmF2 estimated by IRI-2016 URSI is consistent with that of the IRO dataset in terms of the general trend in the typical ionospheric characteristics; except for some discrepancies in the marine area, the IRO data may provide a feasible reference for IRI estimation in marine regions. The hmF2 options of BSE/AMTB/SHU show hemispheric asymmetry like the IRO dataset. Moreover, hmF2 of BSE/AMTB and IRO/SHU show some discrepancies in fine structures, such as the day–night reversal phenomenon.

INDEX TERMS Ionosphere, radio occultation, FY3C, COSMIC, IRI-2016, comparison, NmF2, hmF2.

I. INTRODUCTION

The upper atmosphere is dissociated and ionized by extreme ultraviolet (EUV) and X-ray radiations, which is the main reason for ionosphere formation. Due to the prevalence of gravity, the ionosphere produces different horizontal layered structures composed of varying plasma densities, such as D, E, F1, and F2 regions [1]. The F2 layer is a region with the most severe ionization and is most dynamic in terms of the electron density. The maximum electron density in the F2

The associate editor coordinating the review of this manuscript and approving it for publication was Shunfeng Cheng.

layer, NmF2 (el/m^3), is closely related to the critical F2-layer frequency, foF2 (MHz), as shown in (1):

$$NmF2 = 1.24 \times 10^{10}(foF2)^2 \quad (1)$$

The height of NmF2 (hmF2) is equally significant, as it can be used as an essential data source for constructing neutral winds in mid-latitudes and meridional winds on a global scale [2], [3].

A timely and effective acquisition of the ionospheric parameters, such as foF2 (NmF2) and hmF2, is vital for observing ionospheric behaviors. Hence, various excellent ionospheric models have been developed, such as the NeQuick model [4], Global Assimilation of Ionospheric Measurements (GAIM) model [5], and International Reference Ionosphere (IRI) model [6]. Among these, the IRI model can provide ionospheric parameters, including but not limited to the density of the electrons, their temperatures, and vertical total electron density (VTEC), given the corresponding time and geographical location. As an empirical model, the IRI absorbs almost all available space-based and ground-based ionospheric data including those from the global network of ionosondes/digisondes, incoherent scattering radars (ISRs), ionospheric topside sounders, in situ payloads, and occultation satellites [7]. With more than 20 years of refinement, the IRI model has been internationally recognized as a standard ionospheric model by the International Standardization Organization (ISO) [8]. The IRI model has been updated to the 2016 version, in which foF2 has two model options to choose from, namely the Comite Consultatif International des Radiocommunications (CCIR) and the International Union of Radio Science (URSI), with the CCIR developed by Jones and Roger [9] and the URSI developed by Rush *et al.* [10]. Both the options are based on the 12-month running mean of the global ionosonde (IG) index, namely the IG_{12} index, which enables the mapping of ionosonde foF2 to model foF2. The URSI utilizes a physical model for the foF2 calculation over regions not covered by the ionosonde, instead of using extrapolation methods such as the CCIR. As such, the CCIR is recommended for continents, whereas the URSI is recommended for oceans and is set as the default foF2 option in IRI-2016. The hmF2 option, namely Bilitza-Sheikh-Eyfrig (BSE)-1979 in the old version of the IRI model, is based on the relationship between hmF2 and M(3000)F2, which has a dependency on the 12-month running mean of the sunspot number, R_{12}. The IRI-2016 model adopts two new hmF2 options. One is the Altadill–Magdaleno–Torta–Blanch (AMTB)-2013 model [11], which works through 610 model coefficients under two selected levels of R_{12} based on observation data of 26 digisondes from 1998 to 2006. Another is the SHUbin (SHU)-2015 model developed by Shubin [12], which works through 85824 coefficients under two selected levels of $F_{10.7\_81}$(81-day running mean of the solar radio flux at a wavelength of 10.7 cm) derived from digisonde data and a vast amount of ionospheric radio occultation (IRO) data including Constellation Observing System for Meteorology Ionosphere and Climate (COSMIC). All the three models were developed using data averages during different months (season) and local time (universal time) under high and low solar activities [13].

The IRI-2016 model for the first time adopts the model option of hmF2 based on the IRO data; this is similar to the IRO technique in terms of the excellent performance in retrieving the electron density profiles (EDPs) of the ionosphere. In 1995, the success of the US Microlab-1 low earth orbit (LEO) satellite (GPS/MET) theoretically and technically confirmed the feasibility of the Global Positioning System (GPS) radio occultation technique for observing the Earth's atmosphere and ionosphere for the first time [14]. Since then, the Global Navigation Satellite System (GNSS) IRO technique has shown advantages such as high accuracy, global coverage, high vertical-resolution, high precision, all-weather operation, low cost, and long-term stability [15], [16]. Multiple occultation projects have been implemented: COSMIC, German Challenging Minisatellite Payload (CHAMP), Gravity Recovery and Climate Experiment (GRACE), Communications/Navigation Outage Forecasting System (C/NOFS), and FengYun 3C/D-GNSS Occultation Sounder (FY3C/D-GNOS) [16]–[20]. Launched in 2006, COSMIC is the first six microsatellite constellation with a GPS occultation receiver onboard. It has produced more than 7 million atmospheric/ionospheric occultation events thus far. NmF2 and hmF2 between COSMIC IRO measurements and ionosondes show standard deviations (STDs) of 8.42% and 11.46 km, respectively [21]. The continuous and high-precision occultation observations by COSMIC provide abundant and reasonable support for atmospheric/ionospheric climatology research [22], [23], numerical weather prediction [24], model data assimilation [25], [26], and space weather monitoring [27]. COSMIC significantly accelerates the operationalization of the ionospheric occultation observation; thus, it has a milestone significance in the ionosphere field. Inspired by COSMIC, China has also been developing domestic operational occultation projects, such as FY3C-GNOS, for atmosphere and ionosphere observations. The GNOS developed by National Space Science Center (NSSC) for the 836 km sun-synchronous orbit has obtained a large amount of IRO data since its launch onboard the FY3C satellite in 2013, which is the first GNOS payload compatible with both GPS and BeiDou Navigation Satellite System (BDS) signals in the world. It is capable of tracking signals of 6 GPS and 4 BDS satellites simultaneously and can receive up to 700 occultation events per day (500GPS + 200BDS) [28]. Many studies have evaluated the accuracy of FY3C-GNOS IRO products [15], [16], [29], [30]. For example, Mao *et al.* [29] found that the root-mean-square (RMS) values of the EDPs between FY3C-GNOS GPS IRO and COSMIC/ionosondes are 10%/7%, respectively, demonstrating the precision consistency of the EDP among FY3C-GNOS, COSMIC, and ionosondes. Bai *et al.* [30] also found decent unbiasedness in the statistical difference and ionospheric climatology of NmF2/hmF2 between COSMIC and FY3C-GNOS, which showed an overall systematic offset

of −2.19% for NmF2 and −3.29 km for hmF2. The large amount of FY3C-GNOS IRO data can be a great source of ionospheric climatology, radio communication, and vital precursor information for earthquakes and other hazards [31].

At the time of the IRI-2016 model release, Bilitza *et al.* [6] observed that in the solar cycle from 1958 to 2015, hmF2 estimated by AMTB is approximately 40–50 km higher than that estimated by the BSE option in the low solar activity (LSA) period. Solar cycle 24 has unique characteristics, such as deeper and longer LSA periods than the past hundred years, which has led to significant interest in the research community to evaluate the performance of the IRI-2016 model during this period [32]. For example, Liu *et al.* [33] compared foF2 estimations obtained using IRI-2016 with that of ionosondes in the northern mid-latitude region during a long timescale ranging from 2008 to 2016. The results showed that IRI-2016 can well reproduce foF2 variations with respect to latitude, season, and local time. Rao *et al.* [34] collected foF2 estimated by IRI-2016 and compared it with that of ionosondes in southern low-latitudes during the solar ascending phase from 2009 to 2013. The results showed an overall foF2 consistency between IRI-2016 and ionosondes, with foF2 inconsistency reaching 5 MHz under certain conditions. Similarly, during the ascending solar phase from 2009 to 2014, Patel *et al.* [32] showed that IRI-2016 can more reasonably predict NmF2 than ionosondes for the Indian sector. Furthermore, during the LSA period from 2007 to 2009, Karia *et al.* [35] analyzed the climatological performance of IRI-2016, in which the nighttime winter anomaly (NWA) and Weddell Sea anomaly (WSA) were not evidently reflected in IRI-2016 NmF2.

The above studies have covered the comparisons of ionospheric F2-layer peak parameters, such as NmF2 (foF2) and hmF2, estimated by IRI-2016 at different time scales. Most of them were concentrated in the first solar minimum period and the solar ascending phase in solar cycle 24 from 2008 to 2019, with very few comparisons during the recent second solar minimum period at the end of solar cycle 24. Moreover, most works were conducted with ground-based ionosonde/digisonde measurements. We compared NmF2/hmF2 estimated by IRI-2016 with high-precision IRO data during the second LSA period from 2017 to 2019 in solar cycle 24. As a highly recognized standard in the ionospheric occultation observation field, COSMIC data were selected as the comparative IRO dataset for IRI-2016. Because of its performance degradation in obtaining occultation events after 2014 [36], the occultation data of FY3C-GNOS, which slightly deviate from COSMIC data, were also added to the IRO dataset. Specifically, there are currently two foF2 model options: CCIR and URSI. Since the global climatological characteristics of IRI-2016 are also included in the comparison, we slightly favored the URSI model. Among the three hmF2 model options (BSE, AMTB, and SHU) of IRI-2016, the BSE and AMTB options are based on ionosonde/digisonde data, whereas the SHU option assimilates IRO data as well as digisonde observations. Since the SHU option absorbs IRO data, including COSMIC, there is a concern that the SHU option may be correlated with the COSMIC data used in this study. However, the time interval of COMSIC data assimilated by the SHU option is 2007–2011 [12], whereas the time period of COSMIC data utilized in this work is 2017–2019. Evidently, these intervals are different and far apart, so we still included the SHU option in the comparison. To better represent the uncertainty in the three options in estimating hmF2 and explore how they differ from each other, we carried out a statistical analysis and a climatology comparison of hmF2 between IRO dataset and BSE/AMTB/SHU options of IRI-2016. NmF2 between IRO dataset and IRI-2016 was evaluated using the same method.

The rest of this paper is organized as follows. Section II presents the screening method for the IRO data, the acquisition of the statistical differences in NmF2/hmF2 between IRI-2016 and IRO data, and the binning method of NmF2/hmF2 for climatology comparison. In Section III, we present the statistical deviations in NmF2/hmF2 between IRI-2016 and IRO data. Based on the binning method, we compared the climatological characteristics of NmF2/hmF2 obtained using IRI-2016 and IRO data in Section IV. In Section V, we summarize the statistical differences and climatological characteristics, and discuss the mechanisms behind some of the phenomena observed in this study. Brief conclusions are given in Section VI.

II. MATERIALS AND METHODS

A. SELECTION OF THE IONOSPHERIC RADIO OCCULTATION DATA

Solar cycle 24 (2008–2019) was the weakest period of solar activity in nearly a century with a longer than expected LSA duration [32], which has aroused broad interests in the ionospheric research community. The geomagnetic and solar activities during this period can be characterized using the global geomagnetic activity index (Kp) and the solar radio flux at a wavelength of 10.7 cm ($F_{10.7}$), as shown in Figs. 1a and b, respectively. The Kp and $F_{10.7}$ indices can be accessed from https://omniweb.gsfc.nasa.gov/form/dx1.html of Space Physics Data Facility (SPDF). Generally, the period when Kp is less than or equal to 4 corresponds to the geomagnetic quiet period, and a period of $F_{10.7}$ below 80 is typically defined as the LSA period [37]. Fig. 1b shows that the period from 2017 to 2018 corresponds to the second LSA period in solar cycle 24. Fig. 1a shows that the geomagnetic quiet period accounts for 98.22% in this period, which is an ideal time interval for IRI-2016 comparison with the IRO dataset. More specifically, to present the seasonal patterns of the climatological characteristics of NmF2/hmF2 in ME-month (±45 days to March equinox), JS-month (±45 days to June solstice), SE-month (±45 days to September equinox), and DS-month (±45 days to December solstice) during the LSA period, the IRO data during 2017.035 and 2019.035 were selected as the comparative dataset for IRI-2016. However, COSMIC, which has exceeded its

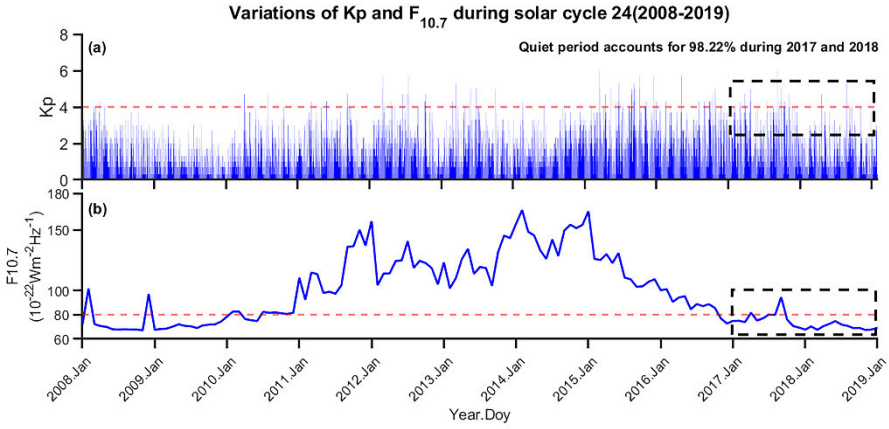

FIGURE 1. Geomagnetic and solar activities during solar cycle 24 from 2008 to 2019. (a) Daily variation in the geomagnetic index Kp from 2008 to 2019. The red dashed line represents a Kp value of 4, namely the critical value of a geomagnetic storm, and the geomagnetic quiet period accounts for 98.22% during the time phase from 2017 to 2018, surrounded by the black dashed box. (b) Monthly mean solar flux index $F_{10.7}$ during solar cycle 24. The red dashed line corresponds to an $F_{10.7}$ value of 80, namely the LSA period threshold, the time phase from 2017 to 2018 is similar to the first LSA period during 2008–2009 in solar cycle 24.

working life, is currently facing severe performance degradation issues. Considering the deterioration in the COSMIC occultation data, we combined the IRO data of COSMIC and FY3C-GNOS to expand the comparison dataset of IRI-2016. The EDP data of COSMIC and FY3C-GNOS can be accessed from https://cdaac-www.cosmic.ucar.edu of COSMIC Data Analysis and Archive Center (CDAAC) and http://satellite.nsmc.org.cn/PortalSite/Data/Satellite.aspx?currentculture=en-US of National Satellite Meteorological Center (NSMC), respectively.

Before comparison, the IRO dataset, including COSMIC and FY3C-GNOS, should be quality controlled. Referring to the methods applied in other studies [12], [15], [38], [39] and our requirement for sample quantity in statistical and climatological analyses, we examined the IRO dataset using four parameters: hmF2 (200–450 km), mean deviation of the EDP fluctuation (MD) (0–0.1), the gradient of the topside EDP (-7×10^6 m^{-4} to -0.1×10^6 m^{-4}), and noise level factor (0–0.01). Moreover, the EDPs were discarded during the geomagnetic storm period when Kp was greater than 4 to avoid data distortion due to the response of NmF2/hmF2 to geomagnetic disturbances.

Yang *et al.* [38] found that ionospheric irregularities can cause EDP fluctuations and even lead to a sharp spike. There are some EDPs in which the topside electron density does not show a decreasing trend but positive or zero gradients. To avoid the above EDPs from mixing in the IRO data application, Yang *et al.* [38] defined the MD index and gradient of the topside EDP to remove the unqualified IRO EDP data. Their definitions are expressed in (2) and (3) as follows:

$$MD = \sum_i \frac{|n_{ei} - \overline{n_{ei}}|}{N\overline{n_{ei}}} \tag{2}$$

where N is the total number of electron density sampling points in a profile. n_{ei} and $\bar{n_{ei}}$ represent the inversion value of the electron density at the i-th sampling point and n_{ei} processed using the 9-point running average filtering method, respectively.

$$Gradient = \frac{n_e(490km) - n_e(420km)}{70km} \tag{3}$$

where n_e(490 km) and n_e(420 km) are the electron densities at 490 km and 420 km, respectively.

Guo *et al.* [39] defined the noise level Delta to eliminate bad-quality EDP data, and its calculation is as follows:

$$Delta = \sqrt{\frac{\sum_{i=1}^{k} (n_e(i) - \overline{n_e}(i))^2}{k(NmF2)^2}} \tag{4}$$

where $n_e(i)$ is the electron density above 300 km, $\bar{n_e}(i)$ represents the smoothed $n_e(i)$, and k is the number of electron density sampling points above 300 km in a profile.

The statistics show that approximately 80% EDPs of the COSMIC and FY3C-GNOS have hmF2, MD, and topside gradient between 200 and 450 km, 0 and 0.1, and -7×10^6 and -0.1×10^6 m^{-4}, respectively, and have Delta less than 0.01. Fig. 2 shows the statistical distributions of the above four parameters of the IRO EDPs. After applying the data screening criterion, 34290 (71.06%) of 48256 COSMIC IRO data pairs and 55668 (70.92%) of 78492 FY3C-GNOS IRO data pairs were screened for later NmF2/hmF2 comparisons with the IRI-2016 model. The number of qualified IRO EDPs of COSMIC and FY3C-GNOS are described in Fig. 3.

B. STATISTICAL DEVIATIONS OF NMF2/HMF2 BETWEEN IRI-2016 AND IRO DATA THROUGH STATISTICAL ANALYSIS

The statistical analysis of NmF2/hmF2 between IRI-2016 and IRO dataset is performed by dividing into three periods: whole day, daytime (0600-1800LT), and nighttime (1800-0600LT). NmF2 in the IRO dataset is compared with the corresponding NmF2 generated by the IRI-2016 URSI

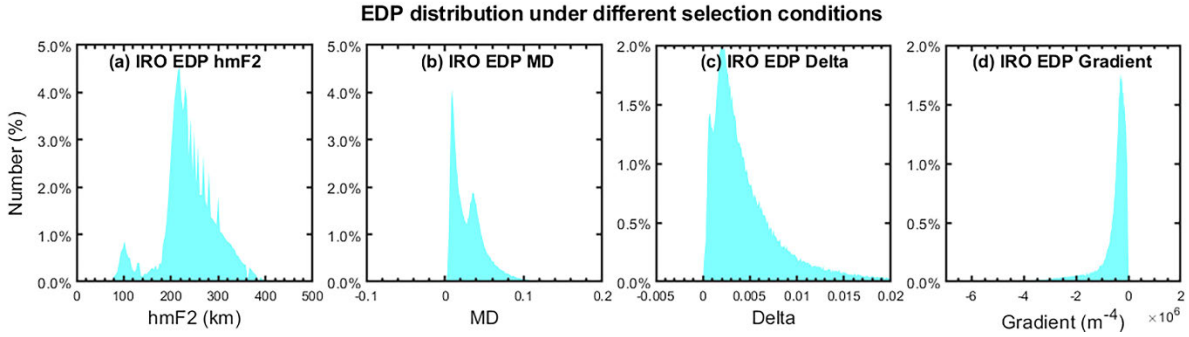

FIGURE 2. Statistical probability distribution of hmF2 (a) MD, (b) Delta, (c) and topside gradient (d) in IRO EDP dataset, including COSMIC and FY3C-GNOS, during the solar minimum from 2017.035 to 2019.035.

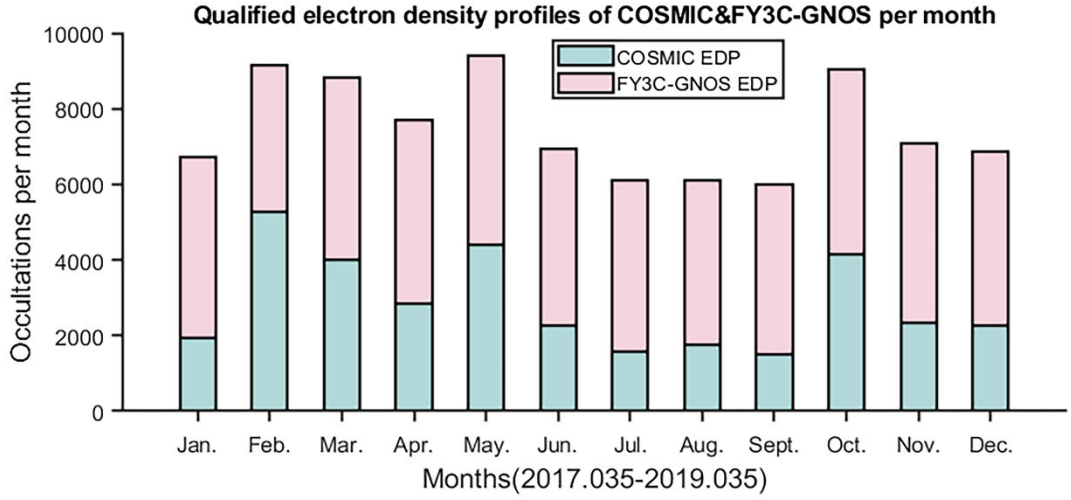

FIGURE 3. Quality controlled IRO EDPs during the solar minimum from 2017.035 to 2019.035, in which the qualified EDPs selected from the COSMIC dataset (green bar) and FY3C-GNOS dataset (red bar) are presented.

option, whereas IRO hmF2 is compared with that estimated by the BSE/AMTB/SHU option in IRI-2016. Considering that the diurnal variation in NmF2 may exceed an order of magnitude, the relative differences in NmF2 between the IRI-2016 and IRO dataset are calculated through NmF2 analysis, and the absolute differences are computed through hmF2 analysis. Based on these, the bias and STD of NmF2/hmF2 relative/absolute differences are calculated as the degree of deviation between IRO and IRI-2016. The detailed derivation method of the bias and STD can be found in the work by Bai *et al.* [30].

C. BINNING METHOD OF NMF2/HMF2 OF IRI-2016 AND IRO DATA FOR CLIMATOLOGY COMPARISON

In addition to presenting NmF2/hmF2 in four different seasons as mentioned in Section II. A, we separated NmF2/hmF2 into daytime (0800-1200 LT) and nighttime (2000-2400 LT) sectors in each season to observe the diurnal variation in the climatological features. To ensure that the number of NmF2/hmF2 readings inside one grid larger than five can occupy more than 70% of the entire grid within $\pm 60^\circ$ in geographical latitudes, we adopted a $3^\circ \times 6^\circ$ grid in this work. Notably, NmF2/hmF2 of IRI-2016 is generated on the basis of the position and local time of the grid center, so the number of NmF2/hmF2 estimations is much higher than that in the IRO dataset. Therefore, the season-averaged NmF2/hmF2 in one grid was derived to represent its NmF2/hmF2 level, to reduce discrepancies due to the data quantity between IRI-2016 and IRO dataset. The ionospheric climatology of season-averaged NmF2/hmF2 in each subset is smoothed using the method proposed by Garcia [40].

III. STATISTICAL DIFFERENCES IN NMF2/HMF2 BETWEEN IRI-2016 AND IRO DATASET

A. STATISTICAL ANALYSIS OF IRI-2016 NMF2 WITH IRO DATASET

Figs. 4a, b, and c show comparisons of NmF2 between IRI-2016 URSI option and IRO dataset during the whole day, daytime, and nighttime from 2017.035 to 2019.035, respectively. After applying the data selection condition presented in Section II.A and the deviation acquisition method presented in Section II.B, we can see in Fig. 4a that there are 89387 NmF2 data pairs between IRI-2016 and IRO dataset during the whole day, in which the correlation

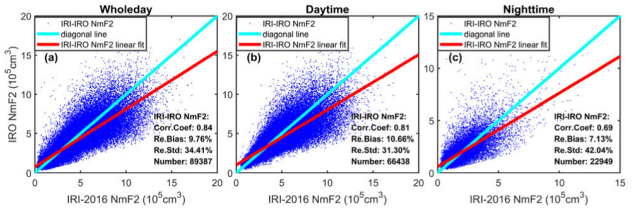

FIGURE 4. Statistical differences in NmF2 between IRI-2016 and IRO dataset from 2017.035 to 2019.035. (a, b, c) Correlations of NmF2 between IRI-2016 and IRO dataset during the whole day, daytime (0600-1800LT), and nighttime (1800-0600LT), respectively. The solid red line represents the linear regression fit of NmF2 between the IRI-2016 and IRO dataset, and the solid blue line describes the diagonal. The correlation coefficient of NmF2 between IRI-2016 and IRO dataset, the bias and STD of NmF2 relative differences, and the number of NmF2 data pairs are labeled in the lower right corner of each panel.

coefficients of NmF2, bias, and STD of NmF2 differences are 0.84, 9.76%, and 34.41%, respectively. Similarly, during daytime, the correlation coefficient, bias, STD, and number of NmF2 estimations between IRI-2016 and IRO dataset are 0.81, 10.66%, 31.30%, and 66439, respectively. In nighttime, the correlation coefficient, bias, STD, and number are 0.69, 7.13%, 42.04%, and 22949, respectively.

In terms of the linear fit and diagonal line of NmF2, we can see that IRI-2016 always overestimates the IRO NmF2. The bias varying from 7.13% to 10.66% is approximately 20%–30% lower than the STD in the range of 31.30%–42.04%, indicating a relatively small significance of the NmF2 systematic offset between IRI-2016 and IRO dataset. Moreover, the NmF2 values of IRI-2016 and IRO are more consistent during daytime, with the correlation coefficient being above 0.8, whereas at nighttime, the correlation coefficient is only 0.69.

B. STATISTICAL ANALYSIS OF IRI-2016 HMF2 WITH IRO DATASET

Figs. 5a, b, and c show the statistical analyses of hmF2 between BSE option of IRI-2016 and IRO dataset, carried out during the whole day, daytime, and nighttime from 2017.035 to 2019.035, respectively. Likewise, the statistical analysis of hmF2 between AMTB/SHU option of IRI-2016 and IRO dataset is presented in Figs. 5d,e,f/g,h,i, respectively.

From the relationship between the linear fit and the diagonal line of hmF2, we see that IRI-2016 shows a higher estimation than IRO observations except for the SHU option, particularly the AMTB option, at nighttime. The three options of IRI-2016 show similar diurnal variations, such as in NmF2, compared with the IRO dataset, i.e., relatively small hmF2 discrepancies between IRI-2016 and IRO dataset during daytime and a relatively weak consistency at nighttime. Judging by the correlation coefficient, bias, and STD, the IRO hmF2 exhibits the best agreement with the SHU option, followed by the BSE option, and then the AMTB option. Although the bias and STD of hmF2 between BSE/AMTB and IRO dataset are largely the same during daytime, at nighttime, the systematic offset of hmF2 between AMTB and IRO data

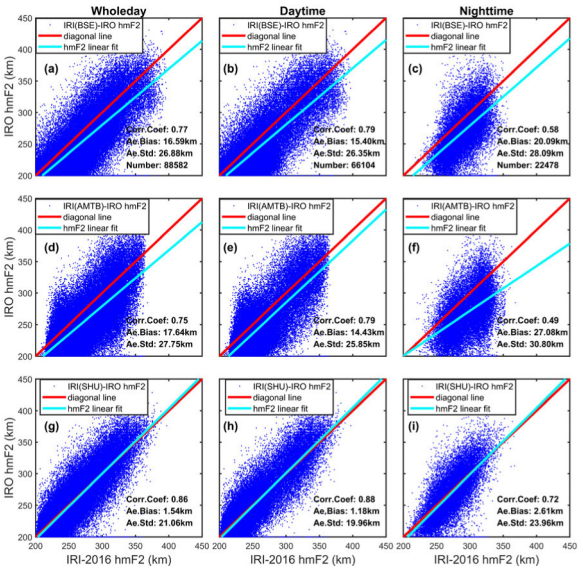

FIGURE 5. Statistical differences in hmF2 between BSE/AMTB/SHU option of IRI-2016 and IRO dataset from 2017.035 to 2019.035. (a, b, c) Correlations of hmF2 between the BSE option of IRI-2016 and IRO dataset during whole day, daytime (0600-1800LT), and nighttime (1800-0600LT). (d, e, f) Correlations of hmF2 between AMTB option of IRI-2016 and IRO dataset during three different periods. (g, h, i) Correlations of hmF2 between SHU option of IRI-2016 and IRO dataset during three different periods. More detailed explanations can be seen in Fig. 4.

increased significantly. Moreover, during the daytime, the hmF2 estimations of BSE have more values scattered within 350–400 km than that of AMTB. More detailed discussions are made in Section V.

IV. IONOSPHERIC CLIMATOLOGICAL CHARACTERISTICS OF NMF2/HMF2 OF IRI-2016 AND IRO DATASET

A. COMPARISON OF THE GLOBAL SEASON-AVERAGED NMF2 IN IONOSPHERIC CLIMATOLOGY

Based on the binning method described in Section II.C, the season-averaged NmF2 of IRI-2016 and IRO dataset at daytime and nighttime and their relative differences in ME-month, JS-month, SE-month, and DS-month are presented in Figs. 6–9, respectively. Thus, the ionospheric climatological characteristics of NmF2 of IRI-2016 and IRO dataset can be intuitively seen as follows.

1) MIDLATITUDE SUMMER NIGHTTIME ANOMALY

The mid-latitude summer nighttime anomaly (MSNA) reveals an abnormal increase in the electron density at nighttime in summer mid-latitude regions [41]. The diurnal NmF2 reaches its maximum during the day due to the strong photochemical control. However, an unusual enhancement in NmF2 occurred at nighttime in the southern summer hemisphere near the Weddell Sea area (52°S, 60°W-75°S, 30°W), which is defined as the Weddell Sea Anomaly (WSA) [42]. With the development of space-based ionospheric observations, a spatial expansion of the WSA to the adjacent area has been observed; for example, Horvath and Essex [43]

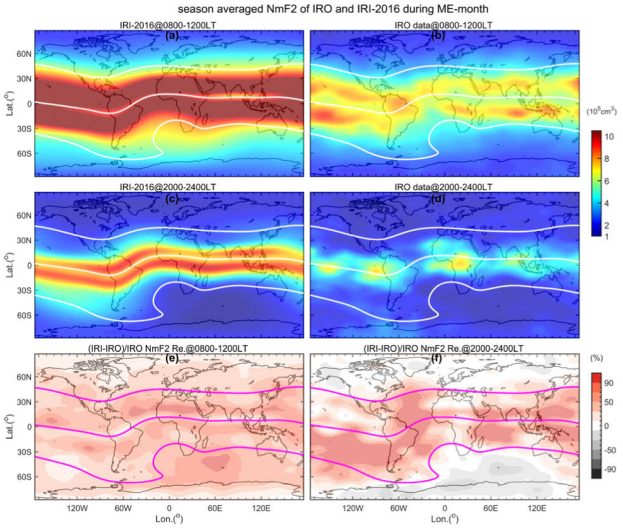

FIGURE 6. Ionospheric climatology of the season-averaged NmF2 of IRI-2016 and IRO dataset in March equinox (ME-month) and their relative differences in the daytime (0800-1200LT) and nighttime (2000-2400LT). (a, b) Ionospheric climatological characteristics of NmF2 of IRI-2016 and IRO subset during 0800-1200LT, respectively. (c, d) Ionospheric climatological features of NmF2 by IRI-2016 and IRO subset during 2000-2400LT, respectively. The three white curves from top to bottom in a-d represent the contours denoted by 60°, 0°, and −60° dips, respectively. (e, f) Relative differences in NmF2 between IRI-2016 and IRO subset during daytime and nighttime, respectively, in which the dip contours are the pink curves.

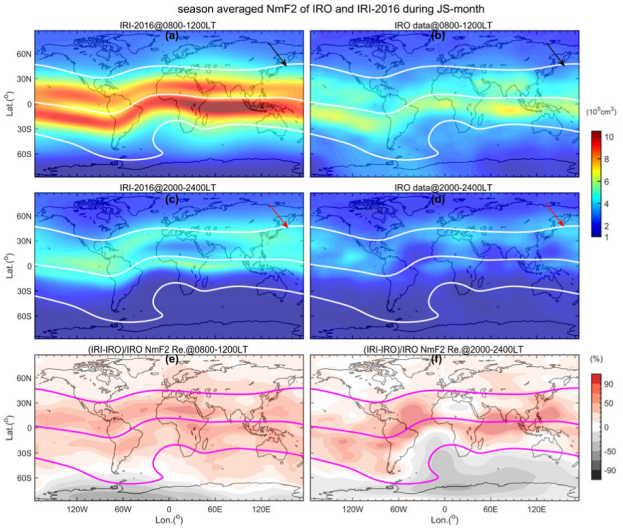

FIGURE 7. Ionospheric climatology of the season-averaged NmF2 of IRI-2016 and IRO subset in June solstice (JS-month) and their relative differences in the daytime (0800-1200LT) and nighttime (2000-2400LT). The arrows indicate the northern MSNA in the diurnal variation in NmF2, in which the area indicated by red arrows in c,d shows the nighttime NmF2 enhancement in comparison to the daytime NmF2 denoted by black arrows in a,b. Refer to Fig. 6 for additional descriptions.

reported TEC enhancement in the southeast Pacific Ocean and the southwest Atlantic Ocean near the WSA region in TOPEX/Poseidon measurements. The enhancement in NmF2 in the northern summer hemisphere has also been observed in various types of ionospheric data; He *et al.* [44] reported NmF2 increase in the mid-latitudes of the northern hemisphere at summer nighttime through COSMIC IRO data.

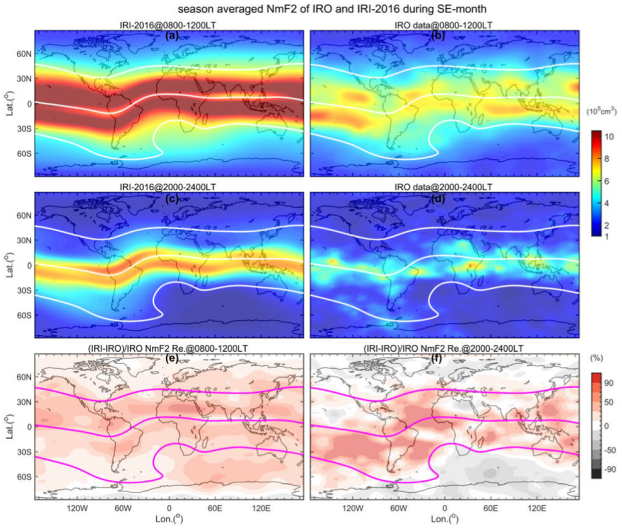

FIGURE 8. Ionospheric climatology of the season-averaged NmF2 of IRI-2016 and IRO subset in September equinox (SE-month) and their relative differences in the daytime (0800-1200LT) and nighttime (2000-2400LT). Refer to Fig. 6 for additional descriptions.

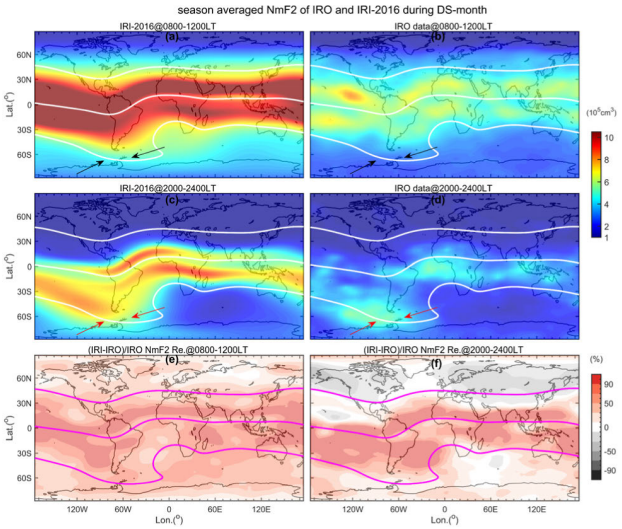

FIGURE 9. Ionospheric climatology of the season-averaged NmF2 of IRI-2016 and IRO subset in December solstice (DS-month) and their relative differences in the daytime (0800-1200LT) and nighttime (2000-2400LT). The arrows indicate the southern MSNA in the diurnal variation in NmF2. Refer to Fig. 7 for additional descriptions.

Among the above nighttime NmF2 enhancement phenomena, the NmF2 increase in the Weddell Sea area is defined as the special WSA, indicated by arrows in Fig. 9c-d, and the NmF2 enhancement in the other areas is called the general WSA, indicated by arrows in Figs. 7, 9c-d [44]. Since the two types of WSAs mostly occur at summer nighttime in mid-latitudes (approximately ± 60° dip) and longitude sector where the magnetic equator shifts farthest toward the geographic poles, both the WSAs are MSNAs.

From Figs. 7, 9a–d, the NmF2 values of IRI-2016 and IRO dataset both show MSNA characteristics. In the northern summer hemisphere (Figs. 7a–d), the NmF2 nighttime enhancement appears in the Northeast Asian sector during

2000-2400LT, which corresponds to the longitude sector where northern MSNA occurred as reported by He *et al.* [44]. Moreover, in the southern summer hemisphere (Figs. 9a–d), we see that NmF2 values of IRI-2016 and IRO during 2000-2400LT present southern MSNA characteristics, including nighttime NmF2 enhancement in the Weddell Sea region and adjacent area. The IRI-2016 and IRO data are consistent in terms of the overall MSNA characteristics in both summer hemispheres, though there is a discrepancy in that the MSNA of IRI-2016 is slightly higher than that of the IRO dataset, particularly in the December solstice.

2) ANNUAL ANOMALY

When the northern and southern hemispheres are considered as a whole, the phenomenon of daytime/nighttime NmF2 in December solstice being more pronounced than that in summer solstice is called the annual anomaly [45]. Taking northern and southern hemispheres as a whole, the NmF2 values of IRI-2016 and IRO dataset are more pronounced in winter solstice than that in summer solstice regardless of whether it was daytime or nighttime. However, NmF2 of IRI-2016 in winter solstice is approximately 50% higher than that in summer solstice. This exceeds the 20%–30% proportion of the typical annual anomaly characteristics [45], [46]. In winter solstice, the IRO NmF2 is approximately 16%–34% higher than that in summer solstice within daytime and nighttime sectors, consistent with the ionospheric characteristics of the annual anomaly.

3) EQUATORIAL IONOSPHERIC ANOMALY

Equatorial ionospheric anomaly (EIA) is an ionospheric sandwich structure of the electron density trough along the magnetic equator surrounded by two high-value electron density crests [47].

The NmF2 values of IRI-2016 and IRO dataset both show distinct EIA features at daytime in the four seasons but with a different seasonal pattern. The EIAs estimated by IRI-2016 show good structural continuity in the four seasons, with a decrease in intensity only during the summer solstice. Meanwhile, the IRO NmF2 declined in terms of the EIA structural continuity in solstices compared to that in equinoxes, showing stronger and weaker seasonal patterns of E×B in equinoxes and solstices, respectively. This is consistent with the seasonal variations in the NmF2 measurements made by ROCSAT-1 as reported by Fejer *et al.* [48]. However, this seasonal pattern of the EIA is not as apparent in IRI-2016 as the IRO dataset.

4) WINTER ANOMALY

The ionospheric phenomenon, where the daytime NmF2 at mid-latitudes in the winter hemisphere is higher than that in the summer hemisphere, is the winter anomaly [45]. Figs. 7, 9a, b show that more pronounced NmF2 of IRI-2016 and IRO mainly appears in equatorial and low-latitude regions in the winter hemisphere. The NmF2 enhancement in the winter anomaly in mid-latitudes tends to subside. Notably, in the first deep solar minimum of solar cycle 24, the same daytime NmF2 enhancements in the low and equatorial regions occurred in the winter hemisphere during 0700-1200LT [49], which cannot be identified as a typical mid-latitude winter anomaly either. The subsidence or even disappearance of the winter anomaly is related to the lower solar energy input in the LSA period, and the winter anomaly is typically prominent at solar maximum [50].

5) SEMI-ANNUAL ANOMALY

The stronger daytime NmF2/foF2 in equinoxes than in solstices is the semi-annual anomaly [45]. The IRI-2016 and IRO dataset both produce high-value NmF2 in equinoxes than in the summer solstice. IRO data also present relatively low NmF2 in winter solstice than in equinoxes. Nevertheless, NmF2 estimated by IRI-2016 in winter solstice does not show a significant decrease compared with that in equinoxes. The lower IRO NmF2 in solstices than in equinoxes is a typical manifestation of the ionospheric semi-annual anomaly. IRI-2016 also presents semi-annual characteristics of NmF2, expect in the winter solstice.

6) RELATIVE DIFFERENCES IN NMF2 BETWEEN IRI-2016 AND IRO DATASET

Figs. 6–9e, f show the global relative differences in NmF2 between the IRI-2016 and IRO dataset over four seasons at daytime and nighttime. We can observe that NmF2 of IRI-2016 shows a noticeable higher trend relative to that of the IRO dataset, and most of the differences are distributed along the magnetic equator within the ±60° dip, particularly at nighttime.

During daytime, as shown in Figs. 6-9e, the magnitude of the relative differences is slightly lower than that at nighttime within the ±60° dip. However, the daytime difference is spread worldwide, whereas at nighttime, it decreases significantly in mid-high latitudes. Therefore, the NmF2 difference between IRI-2016 and IRO dataset is higher in daytime in the four seasons. Interestingly, IRI-2016 has higher daytime NmF2 than IRO data at the longitude sector southeast of the −60° dip, but shows a lower NmF2 trend at nighttime in this region. The same local-time-dependent characteristics of IRI-2016 NmF2 are also shown in the high latitude area north of the 60° dip, except in the summer solstice.

IRI-2016 has higher NmF2 values in spring equinox and winter solstice. In the daytime of equinoxes, IRI-2016 NmF2 exceeds the IRO NmF2 by approximately 30%–50% in most areas in spring equinox, and the 10%–30% higher fraction of IRI-2016 accounts for a large proportion in autumn equinox. At nighttime, the relative difference in the spring equinox is entirely strengthened in the equatorial region, particularly in the Pacific, Atlantic, and the Indian Ocean sectors, compared to autumn equinox. The relative difference variations in the winter and summer solstices are similar to that in spring and autumn equinoxes. The NmF2 deviation between IRI-2016 and IRO dataset in the winter solstice is

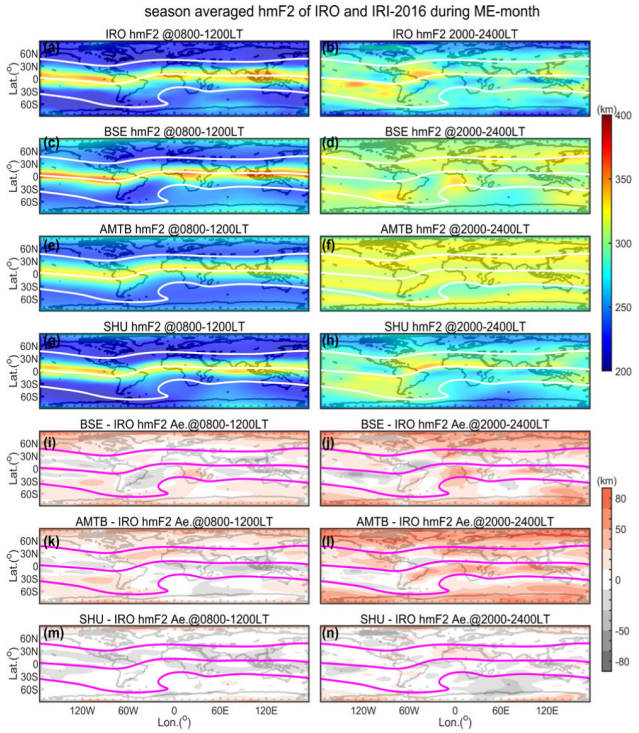

FIGURE 10. Ionospheric climatology of the season-averaged hmF2 of BSE/AMTB/SHU option of IRI-2016 model and IRO dataset in March equinox (ME-month) and their absolute differences at daytime (0800-1200LT) and nighttime (2000-2400LT). (a, b) Ionospheric climatological characteristics of hmF2 by IRO subset during daytime and nighttime, respectively. (c, d) Ionospheric climatological features of hmF2 estimated by the IRI-2016 BSE option during daytime and nighttime, respectively. (e, f) Ionospheric behaviors of hmF2 estimated by the IRI-2016 AMTB option during daytime and nighttime, respectively. (g, h) Ionospheric climatological features of hmF2 estimated by the IRI-2016 SHU option during daytime and nighttime, respectively. The three white curves from top to bottom in (a)-(h) represent the contours denoted by 60°, 0°, and −60° dip, respectively. (i, j) Absolute differences in hmF2 between IRI-2016 BSE and IRO subset during daytime and nighttime, respectively. (k, l) Absolute differences in hmF2 between IRI-2016 AMTB and IRO subset at daytime and nighttime, respectively. (m, n) Absolute differences in hmF2 between IRI-2016 SHU and IRO subset during daytime and nighttime, respectively. The pink curves indicate the dip contours.

significantly enhanced in terms of the magnitude and distribution regardless of whether it was daytime or nighttime compared to the summer solstice.

B. COMPARISON OF THE GLOBAL SEASON-AVERAGED HMF2 IN IONOSPHERIC CLIMATOLOGY

Based on the binning method provided in Section II.C, Figs. 10-13a-f show the global distribution of hmF2 estimated by IRI-2016's BSE/AMTB/SHU option and measured by IRO in ME-month, JS-month, SE-month, and DS-month, respectively. Figs. 10–13i-n also show the absolute differences in hmF2 between them. Compared with NmF2, the seasonal pattern of hmF2 is quite simple, with the annual variation in summer peaking as the main factor [23]. As shown in the above figures, we can intuitively see the ionospheric characteristics and absolute differences between IRI-2016 and IRO as follows.

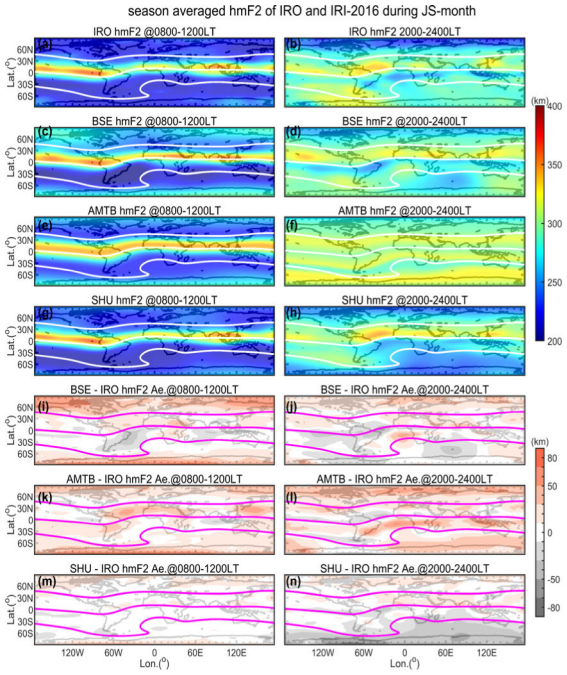

FIGURE 11. Ionospheric climatology of the season-averaged hmF2 of BSE/AMTB/SHU option of the IRI-2016 model and IRO subset in June solstice (JS-month) and their absolute differences at daytime (0800-1200LT) and nighttime (2000-2400LT). More detailed explanations can be found in Fig. 10.

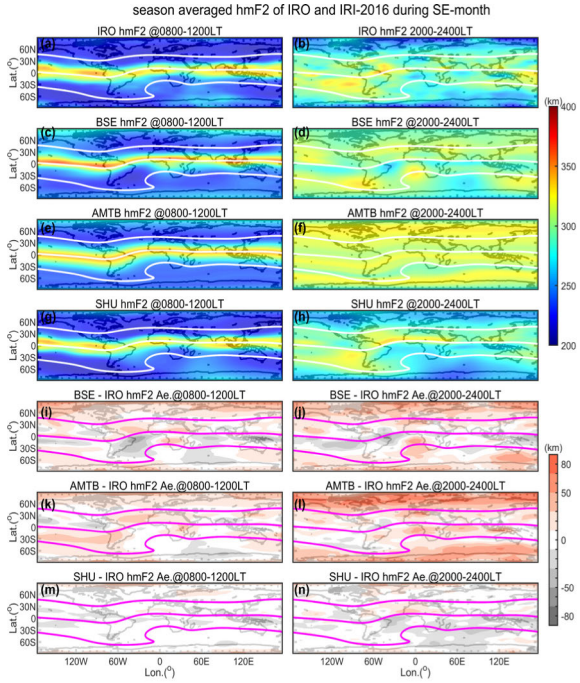

FIGURE 12. Ionospheric climatology of the season-averaged hmF2 of BSE/AMTB/SHU option of IRI-2016 model and IRO subset in September equinox (SE-month) and their absolute differences at daytime (0800-1200LT) and nighttime (2000-2400LT). More detailed explanations can be found in Fig. 10.

1) SEASONAL PATTERN OF HMF2 OF IRO DATASET AND BSE/AMTB/SHU OPTIONS OF IRI-2016

The phenomenon that hmF2 value in the summer hemisphere is higher than that in the winter hemisphere is the

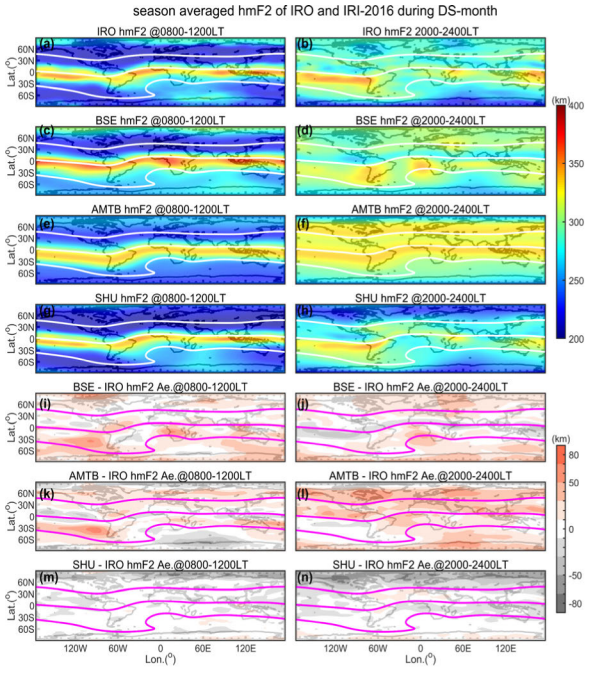

FIGURE 13. Ionospheric climatology of the season-averaged hmF2 of BSE/AMTB/SHU option of the IRI-2016 model and IRO subset in December solstice (DS-month) and their absolute differences at daytime (0800-1200LT) and nighttime (2000-2400LT). More detailed explanations can be found in Fig. 10.

ionospheric hemispheric asymmetry. The hemispheric asymmetry of hmF2 indicates the hemispheric difference in the neutral wind and temperature [51]. We can see that the daytime hmF2 of the three options and daytime hmF2 of IRO all show hemispheric asymmetry in solstices (Figs. 11, 13 a, c, and e). The MSNA phenomenon was also reflected in the global ionospheric hmF2 characteristics estimated by BSE/AMTB/SHU option and measured by the IRO data. Different from NmF2, the hmF2 MSNA also appeared in the winter hemisphere and equinoxes, which means that special and general WSA appear in all four seasons [44]. Nevertheless, because of the relatively small enhancement along the −60° dip, the southern MSNA of nighttime hmF2 exhibited by the AMTB option is not as pronounced as the BSE/SHU option and IRO data.

2) DIURNAL CHARACTERISTICS OF HMF2 OF IRO DATASET AND BSE/AMTB/SHU OPTIONS OF IRI-2016

As shown in Figs. 10–13 a, c, e, during daytime, hmF2 is strongly dip-aligned, showing high-value hmF2 along the magnetic equator, which is reflected in the hmF2 distribution of BSE/AMTB/SHU option and IRO data. At nighttime, as shown in Figs. 10–13 b, d, f, the hmF2 value has a global increase. While in the equatorial region, the enhancement in hmF2 is not as evident and even weakened, which makes the diurnal variation in hmF2 more complicated. At nighttime, the AMTB option has the highest hmF2 enhancement, followed by BSE option and IRO data, and the SHU option is the weakest. Interestingly, at daytime in December solstice, we can see from hmF2 of IRO/SHU that high-value hmF2 is concentrated in the magnetic equatorial region, but another relatively large hmF2 extends southward from the Southern Indian Ocean sector. At nighttime, the higher hmF2 in this area is occupied by lower values again. However, the above day-night reversal phenomenon is not apparent in BSE/AMTB hmF2 in December solstice.

3) ABSOLUTE DIFFERENCES IN HMF2 BETWEEN IRI-2016 AND IRO DATASET

Figs. 10–13i-n show the absolute differences in hmF2 between IRO data and BSE/AMTB/SHU option during daytime and nighttime. Compared to IRO data, BSE and AMTB options both show a higher trend for IRO hmF2 in most regions, whereas the SHU option is generally very close to IRO; however, the trend is lower in some areas. Moreover, the AMTB hmF2 at nighttime has stronger deviations than the BSE option, and the differences in SHU are far smaller than both BSE and AMTB. Unlike NmF2, the hmF2 differences between BSE/AMTB/SHU and IRO are mostly distributed outside the ±60° dip in the mid-high latitudes.

In spring equinox (Figs. 10g–j), at daytime, the 10–30 km hmF2 difference between BSE/AMTB and IRO prevails beyond the ±60° dip. At nighttime, the dominant area increases to 50–70 km outside the ± 60° dip. Within the ±60° dip, almost all the hmF2 deviations show a trend of day–night reversal. The discrepancies in hmF2 are mainly concentrated in the Pacific Ocean, Atlantic Ocean, and Indian Ocean sectors. As far as the SHU option is concerned, the −10–10 km deviation between SHU and IRO occupies most regions, and the IRO hmF2 is evidently underestimated in the south of the −60° dip from 0 and 120 °E. In autumn equinox (Figs. 12i–n), the hmF2 absolute differences in BSE/AMTB are similar to that in the spring equinox except that the day–night reversal of hmF2 differences is not clearly observed, while the range of the lower hmF2 area estimated by SHU is extended.

Different from the equinoxes, within the nighttime of the summer solstice (Figs. 11i–n), the hmF2 difference between BSE option and IRO is significantly reduced in the northern mid-high latitudes, with most regions being dominated by the −10–30 km deviation. The difference in hmF2 between AMTB and IRO at nighttime is not as severe as that in the equinoxes either. During the winter solstice (Figs. 13g–j), the difference in BSE hmF2 also decreases at nighttime compared to daytime, whereas at AMTB, it increases significantly. Compared with the equinoxes, in solstices, the amplitude of the SHU hmF2 underestimation is increased from −10–30 km to −30 to −50 km, whereas the range extends from 0–120°E to the entire longitude section outside the ±60° dip. Interestingly, in the summer solstice, the underestimation part fills the area south of the −60° dip, whereas in winter, it fills the area north of the 60° dip.

TABLE 1. Statistical differences in NmF2 and hmF2 between IRI-2016 estimations and IRO observations at whole day, daytime, and nighttime.

Parameter	Period	Correlation	Bias	Std
URSI NmF2	Whole day	0.84	9.76%	34.41%
	Daytime	0.81	10.66%	31.30%
	Nighttime	0.69	7.13%	42.04%
BSE hmF2	Whole day	0.77	16.59 km	26.88 km
	Daytime	0.79	15.40 km	26.35 km
	Nighttime	0.58	20.09 km	28.09 km
AMTB hmF2	Whole day	0.75	17.64 km	27.75 km
	Daytime	0.79	14.43 km	25.85 km
	Nighttime	0.49	27.08 km	30.80 km
SHU hmF2	Whole day	0.86	1.54 km	21.06 km
	Daytime	0.88	1.18 km	19.96 km
	Nighttime	0.72	2.81 km	23.96 km

V. DISCUSSION

The statistical deviations in NmF2 and hmF2 between IRI-2016 and IRO data are summarized in Table 1. The NmF2 statistical analysis shows that the overall bias and STD of NmF2 between IRI-2016 and IRO dataset are 9.76% and 34.41%, respectively, indicating little significance of the NmF2 systematic offset between IRI-2016 and IRO dataset. In whole day, the correlation coefficient of hmF2, bias, and STD of hmF2 differences are 0.77, 16.59 km, and 26.88 km between BSE and IRO data; 0.75, 17.64 km, and 27.75 km between AMTB and IRO data; and 0.86, 1.54 km, and 21.06 km between SHU and IRO data, respectively. In terms of the correlation coefficient, bias, and STD, the SHU option fits best with the IRO data, and the BSE option is very close to the AMTB option. However, the AMTB option shows a decrease in the correlation coefficient and an increase in the bias at nighttime. Therefore, in summary, the SHU fits best with the IRO, and BSE fits slightly better than AMTB.

Since the SHU option absorbs a large amount of IRO data, it is reasonable that the SHU has the best fit with the IRO data. The consistency between IRO and BSE is slightly better than that between IRO and AMTB. Due to the insufficient harmonic function order (up to 4) and the uncertainty between M(3000)F2 and hmF2 [6], hmF2 estimated by the BSE option cannot reproduce the nighttime hmF2 peak in equatorial regions, like the AMTB option developed from the measured hmF2 dataset. Furthermore, the reliability of the IRO NmF2/hmF2 data will degrade in the equatorial region because of the assumption of the local spherical symmetry in the inversion process, particularly at nighttime [52]. Therefore, when IRO data are fitted with the BSE and AMTB options, it shows a slightly higher agreement with the BSE option, whereas the consistency between IRO and AMTB option declines at nighttime.

The consistency of NmF2/hmF2 between them deteriorated at nighttime compared to daytime, which is an entirely understandable situation. One possible explanation may be that NmF2 is one order of magnitude lower at nighttime than during the daytime, so a smaller absolute difference in NmF2 between IRI-2016 and IRO data at nighttime will be amplified to a higher relative difference, causing a relatively poor NmF2 consistency at nighttime. Moreover, due to the strong photochemistry control at daytime, the modulation effect of ionospheric irregularities on the carrier phase of the GNSS signal, namely the ionospheric scintillation, plays a limited role in the propagation of the occultation rays. However, at nighttime, in the absence of daytime active photochemistry control, there is evident modulation of the ionospheric scintillation on the carrier phases coming from different directions [53]; thus, NmF2 estimated by IRI-2016 mainly based on the ionosonde data will deviate significantly from NmF2 measured by the IRO technique at nighttime.

The ionospheric NmF2 climatological characteristics indicate an overall higher NmF2 obtained using IRI-2016 than the IRO measurements, and the differences are mainly within the $\pm 60^\circ$ dip. The NmF2 deviations between IRI-2016 and IRO are more significant during daytime than at nighttime; moreover, they are greater in spring equinox and winter solstice, and smaller in summer solstice and autumn equinox. Furthermore, most of the differences are concentrated in the Pacific Ocean, Atlantic Ocean, and Indian Ocean sectors, particularly at nighttime. Similar to the global comparison of COSMIC NmF2 with the IRI model in the initial stage of the first LSA period in solar cycle 24, the IRI model shows general features of the IRO measured NmF2, like MSNA, EIA, semi-annual anomaly, and annual anomaly, and the winter anomaly shows signs of disappearance [23], [41], [54]. Regardless of whether in the first or second LSA periods, the IRI model did not show the four-wave longitudinal structures along the dip equator at nighttime in March equinox [54]. Liu *et al.* [23] also found that higher NmF2 values in middle-latitudes over the longitude sector between 60°W–60°E during the March equinox in 2008–2009. However, this was not evident in our work, which may have been due to the particularity of the second LSA period.

Among the ionospheric behaviors, the physical mechanism behind EIA is strongly associated with the electrodynamics arising from the equatorial region. The E $\times$ B drift will lift the ionization compositions to higher altitudes in the equatorial region during the daytime, which is the so-called equatorial fountain effect. Thus, the ionization will spread to higher latitudes along the magnetic field line when being

raised to a certain height under the influences of air pressure and gravity. Since the semi-annual anomaly is mainly reflected in the equatorial region by the sandwiched structure, it can be determined that the semi-annual anomaly is modulated by the seasonal pattern of E×B driving EIA, in which the E×B in equinoxes is stronger than that in solstices as mentioned in Section IV.A.3. Moreover, the upper atmospheric temperature and the semi-annual pattern of the neutral compositions due to the geomagnetic and auroral activities may be factors in forming the semi-annual anomaly [50], [55], [56]. Existing studies on annual anomaly showed that the 7% annual variation in the sun-to-earth distance between June and December solstices plays a vital role in the formation of the annual anomaly, but is insufficient to support the 20%–30% annual variation in NmF2. Therefore, factors, such as the thermosphere's neutral composition and the geomagnetic field configuration, were also considered [57], [58]. However, currently, there are no mechanisms that can thoroughly explain the 20%–30% annual variation in NmF2 between the two solstices in the ionospheric annual anomaly [45], [46].

The hmF2 climatological analysis shows that the hmF2 differences between IRO and IRI-2016 are mainly distributed beyond the ±60° dip. The hmF2 estimations made by the BSE and AMTB options of IRI-2016 show a higher trend in most regions, whereas that made by the SHU option is generally close to the IRO data. The hmF2 differences between BSE/AMTB/SHU and IRO is greater at nighttime than at daytime, and the differences in SHU are far smaller than both BSE and AMTB. Similar to the COSMIC observation in 2008–2009 [23], hmF2 of BSE/AMTB/SHU option and IRO dataset can reveal the ionospheric climatological characteristics like hemispheric asymmetry. The present studies proposed that the hemispheric asymmetry of hmF2 indicates hemispheric difference in the neutral wind and temperature [51]. The strong equatorial wind with hemispheric asymmetry transports the ionization components in the winter hemisphere to the summer hemisphere, thereby increasing the height of NmF2 in the summer hemisphere in solstices [59]. We can also see a notable day–night reversal phenomenon in March equinox and December solstice, as reported in a previous study [23]. The high-value daytime hmF2 east-southward extending from the South Indian Ocean was taken over by the low-value hmF2 at nighttime. During 2017–2019, this feature was more prominent in December solstice and less so in March equinox, though not apparent in BSE and AMTB in December solstice.

Evidently, in terms of the NmF2 climatological characteristics over the four seasons, the NmF2 inconsistency between IRI-2016 and IRO dataset in the northern mid-latitudes is relatively low, particularly at nighttime, which may be related to the sufficient data sources of the IRI-2016 model in the northern mid-latitude region and high applicability of the general law of Abel inversion for the IRO data. The main data sources assimilated into the IRI-2016 model to estimate the ionospheric electron density are from the ground-based ionosondes/digisondes [7], so the dense distribution of the ionosondes in the northern mid-latitudes gives IRI-2016 a relatively high estimation accuracy. The Abel formula to invert the IRO electron densities relies on the local spherical symmetry assumption, and the horizontal uniformity of the electron density in the middle latitude area is comparatively high. Under the effects of these two factors, NmF2 estimated by IRI-2016 in the northern mid-latitude area is more agreeable with that of the IRO dataset.

VI. CONCLUSION

The NmF2/hmF2 model option performance of IRI-2016 was compared with those of IRO data during the recent LSA period from 2017.035 to 2019.035, in terms of the statistical deviations and climatological characteristics. For the statistical analysis, NmF2/hmF2 of IRI-2016 was compared with that of IRO data in terms of the bias and STD in whole day, daytime, and nighttime. For climatological comparison, NmF2/hmF2 values estimated using IRI-2016 and IRO were divided into 3°×6° grids and presented as monthly averages in the daytime and nighttime sectors in the four seasons, to observe the diurnal variation in their climatological characteristics.

The URSI NmF2 estimated by IRI-2016 and NmF2 measured by the IRO technique were generally in agreement, with the systematic offset being less than 10%, and their climatological features tending to be consistent, such as EIA, semi-annual anomaly, annual anomaly, and MSNA. Nevertheless, the higher NmF2 estimations of IRI-2016 led to some climatological inconsistencies in marine areas. The globally distributed IRO data may provide a feasible reference for the monthly-hourly medians of IRI-2016 NmF2 estimations in marine regions. The SHU option for hmF2 estimation showed a better fit to the IRO data compared with the BSE/AMTB option. The BSE/AMTB/SHU option could describe the general trend in the IRO-measured hmF2 with few exceptions. There were some inconsistencies between IRO/SHU and BSE/AMTB in fine hmF2 ionospheric structures, such as the day–night reversal phenomenon, which may have been due to the different hmF2 retrieval methods between them.

With the success of the COSMIC-2 project and the gradual deployment of the Fengyun occultation constellation network, we can assimilate or integrate more quality-controlled IRO data into IRI model in the future, thus helping to improve the estimations made using the IRI model, particularly in marine areas.

ACKNOWLEDGMENT

The authors sincerely thank CDAAC team for providing the COSMIC EDP data (https://cdaac-www.cosmic.ucar.edu/); NSMC for providing the FY3C-GNOS EDP data (http://satellite.nsmc. org.cn/PortalSite/Data/Satellite.aspx); SPDF for providing Kp and $F_{10.7}$ indexes (https://omniweb.gsfc.nasa.gov/form/ dx1.html).

REFERENCES

[1] K. Davies, *Ionospheric Radio*. London, U.K.: IET, 1990, pp. 130–137.
[2] K. L. Miller, D. G. Torr, and P. G. Richards, "Meridional winds in the thermosphere derived from measurement of F2 layer height," *J. Geophys. Res.*, vol. 91, no. A4, pp. 4531–4535, Apr. 1986.
[3] P. L. Dyson, T. P. Davies, M. L. Parkinson, A. J. Reeves, P. G. Richards, and C. E. Fairchild, "Thermospheric neutral winds at southern mid-latitudes: A comparison of optical and ionosondehmF2methods," *J. Geophys. Res., Space Phys.*, vol. 102, no. A12, pp. 27189–27196, Dec. 1997.
[4] B. Nava, P. Coïsson, and S. M. Radicella, "A new version of the NeQuick ionosphere electron density model," *J. Atmos. Solar-Terr. Phys.*, vol. 70, no. 15, pp. 1856–1862, Dec. 2008.
[5] R. W. Schunk, L. Scherliess, J. J. Sojka, D. C. Thompson, D. N. Anderson, M. Codrescu, C. Minter, T. J. Fuller-Rowell, R. A. Heelis, M. Hairston, and B. M. Howe, "Global assimilation of ionospheric measurements (GAIM)," *Radio Sci.*, vol. 39, no. 1, Jan. 2004, Art. no. RS1S02.
[6] D. Bilitza, D. Altadill, V. Truhlik, V. Shubin, I. Galkin, B. Reinisch, and X. Huang, "International reference ionosphere 2016: From ionospheric climate to real-time weather predictions," *Space Weather*, vol. 15, no. 2, pp. 418–429, Feb. 2017.
[7] D. Bilitza, D. Altadill, Y. Zhang, C. Mertens, V. Truhlik, P. Richards, L.-A. McKinnell, and B. Reinisch, "The international reference ionosphere 2012—A model of international collaboration," *J. Space. Weather Space*, vol. 4, Jan. 2014, Art. no. A07.
[8] T. L. Gulyaeva and D. Bilitza, "Towards ISO standard earth ionosphere and plasmasphere model," in *New Developments in the Standard Model*. Hauppauge, NY, USA: Nova, 2012, pp. 1–39.
[9] W. B. Jones and M. G. Roger, "Representation of diurnal and geographic variations of ionospheric data by numerical methods," *Telecommun. J.*, vol. 29, no. 5, pp. 129–147, Jul. 1962.
[10] C. Rush, M. Fox, D. Bilitza, K. Davies, and M. Pokempner, "Ionospheric mapping: An update of foF2 coefficients," *Telecommun. J.*, vol. 56, no. 3, pp. 179–182, 1989.
[11] D. Altadill, S. Magdaleno, J. M. Torta, and E. Blanch, "Global empirical models of the density peak height and of the equivalent scale height for quiet conditions," *Adv. Space Res.*, vol. 52, no. 10, pp. 1756–1769, Nov. 2013.
[12] V. N. Shubin, "Global median model of the F2-layer peak height based on ionospheric radio-occultation and ground-based digisonde observations," *Adv. Space Res.*, vol. 56, no. 5, pp. 916–928, Sep. 2015.
[13] F. Arıkan, U. Sezen, and T. L. Gulyaeva, "Comparison of IRI-2016 F2 layer model parameters with ionosonde measurements," *J. Geophys. Res., Space Phys.*, vol. 124, no. 10, pp. 8092–8109, Oct. 2019.
[14] C. Rocken, R. Anthes, M. Exner, D. Hunt, S. Sokolovskiy, R. Ware, M. Gorbunov, W. Schreiner, D. Feng, B. Herman, Y.-H. Kuo, and X. Zou, "Analysis and validation of GPS/MET data in the neutral atmosphere," *J. Geophys. Res., Atmos.*, vol. 102, no. D25, pp. 29849–29866, Dec. 1997.
[15] G. Yang, Y. Sun, W. Bai, X. Zhang, C. Liu, X. Meng, Y. Bi, D. Wang, and D. Zhao, "Validation results of NmF2 and hmF2 derived from ionospheric density profiles of GNOS on FY-3C satellite," *Sci. China Technol. Sci.*, vol. 61, no. 9, pp. 1372–1383, Mar. 2018.
[16] W. Bai, G. Wang, Y. Sun, J. Shi, G. Yang, X. Meng, D. Wang, Q. Du, X. Wang, J. Xia, Y. Cai, C. Liu, W. Li, C. Wu, D. Zhao, D. Wu, and C. Liu, "Application of the Fengyun 3 C GNSS occultation sounder for assessing the global ionospheric response to a magnetic storm event," *Atmos. Meas. Techn.*, vol. 12, no. 3, pp. 1483–1493, Mar. 2019.
[17] R. A. Anthes, P. A. Bernhardt, Y. Chen, L. Cucurull, K. F. Dymond, D. Ector, S. B. Healy, S. P. Ho, D. C. Hunt, Y. H. Kuo, and H. Liu, "The COSMIC/FORMOSAT-3 mission: Early results," *Bull. Amer. Meteorol. Soc.*, vol. 89, no. 3, pp. 313–334, Mar. 2008.
[18] J. Wickert, C. Reigber, G. Beyerle, R. König, C. Marquardt, T. Schmidt, L. Grunwaldt, R. Galas, T. K. Meehan, W. G. Melbourne, and K. Hocke, "Atmosphere sounding by GPS radio occultation: First results from CHAMP," *Geophys. Res. Lett.*, vol. 28, no. 17, pp. 3263–3266, Sep. 2001.
[19] G. Beyerle, "GPS radio occultation with GRACE: Atmospheric profiling utilizing the zero difference technique," *Geophys. Res. Lett.*, vol. 32, no. 13, 2005, Art. no. L13806.
[20] O. de La Beaujardière, "C/NOFS: A mission to forecast scintillations," *J. Atmos. Sol.-Terr. Phys.*, vol. 66, no. 17, pp. 1573–1591, Sep. 2004.
[21] A. Krankowski, I. Zakharenkova, A. Krypiak-Gregorczyk, I. I. Shagimuratov, and P. Wielgosz, "Ionospheric electron density observed by FORMOSAT-3/COSMIC over the European region and validated by ionosonde data," *J. Geodesy*, vol. 85, no. 12, pp. 949–964, May 2011.
[22] A. G. Burns, S. C. Solomon, W. Wang, L. Qian, Y. Zhang, and L. J. Paxton, "Daytime climatology of ionosphericNmF2andhmF2from COSMIC data," *J. Geophys. Res., Space Phys.*, vol. 117, no. A9, Sep. 2012, Art. no. A09315.
[23] L. Liu, H. Le, Y. Chen, M. He, W. Wan, and X. Yue, "Features of the middle- and low-latitude ionosphere during solar minimum as revealed from COSMIC radio occultation measurements," *J. Geophys. Res., Space Phys.*, vol. 116, no. A9, Sep. 2011, Art. no. A09307.
[24] R. A. Anthes, C. Rocken, and Y.-H. Kuo, "Applications of COSMIC to meteorology and climate," *Terr. Atmos. Ocean Sci.*, vol. 11, no. 1, pp. 115–156, Mar. 2000.
[25] X. Yue, W. S. Schreiner, Y.-H. Kuo, D. C. Hunt, W. Wang, S. C. Solomon, A. G. Burns, D. Bilitza, J.-Y. Liu, W. Wan, and J. Wickert, "Global 3-D ionospheric electron density reanalysis based on multisource data assimilation," *J. Geophys. Res., Space Phys.*, vol. 117, no. A9, Sep. 2012, Art. no. A09325.
[26] S.-P. Ho, X. Yue, Z. Zeng, C. O. Ao, C.-Y. Huang, E. R. Kursinski, and Y.-H. Kuo, "Applications of COSMIC radio occultation data from the troposphere to ionosphere and potential impacts of COSMIC-2 data," *Bull. Amer. Meteorol. Soc.*, vol. 95, no. 1, pp. ES18–ES22, Jan. 2014.
[27] X. Yue, W. Schreiner, Y.-H. Kuo, D. Hunt, and C. Rocken, "GNSS radio occultation technique and space weather monitoring," in *Proc. ION GNSS*, vol. 3, Sep. 2013, pp. 16–20.
[28] Y. Cai, W. Bai, X. Wang, Y. Sun, Q. Du, D. Zhao, X. Meng, C. Liu, J. Xia, D. Wang, D. Wu, W. Li, C. Wu, and C. Liu, "In-orbit performance of GNOS on-board FY3-C and the enhancements for FY3-D satellite," *Adv. Space Res.*, vol. 60, no. 12, pp. 2812–2821, Dec. 2017.
[29] T. Mao, L. Sun, G. Yang, X. Yue, T. Yu, C. Huang, Z. Zeng, Y. Wang, and J. Wang, "First ionospheric radio-occultation measurements from GNSS occultation sounder on the Chinese Feng-Yun 3C satellite," *IEEE Trans. Geosci. Remote Sens.*, vol. 54, no. 9, pp. 5044–5053, Sep. 2016.
[30] W. Bai, G. Tan, Y. Sun, J. Xia, C. Cheng, Q. Du, X. Wang, G. Yang, M. Liao, Y. Liu, X. Meng, D. Zhao, C. Liu, Y. Cai, D. Wang, Y. Wang, C. Yin, P. Hu, and Z. Liu, "Comparison and validation of the ionospheric climatological morphology of FY3C/GNOS with COSMIC during the recent low solar activity period," *Remote Sens.*, vol. 11, no. 22, p. 2686, Nov. 2019.
[31] C. Wang, "Development of the Chinese meridian project," *Chin. J. Space Sci.*, vol. 30, no. 4, pp. 382–384, 2010.
[32] N. C. Patel, S. P. Karia, and K. N. Pathak, "Evaluation of the improvement of IRI-2016 over IRI-2012 at the india low-latitude region during the ascending phase of cycle 24," *Adv. Space Res.*, vol. 63, no. 6, pp. 1860–1881, Mar. 2019.
[33] Z. Liu, H. Fang, L. Weng, S. Wang, J. Niu, and X. Meng, "A comparison of ionosonde measured foF2 and IRI-2016 predictions over China," *Adv. Space Res.*, vol. 63, no. 6, pp. 1926–1936, Mar. 2019.
[34] S. S. Rao, M. Chakraborty, R. Pandey, and A. K. Singh, "FoF2 variability at a southern low-latitude station and the performance of IRI-2016 model during ascending phase of solar cycle-24," *Adv. Space Res.*, vol. 64, no. 11, pp. 2269–2279, Dec. 2019.
[35] S. P. Karia, J. Kim, A. O. Afolayan, and T. I. Lin, "A study on nighttime winter anomaly (NWA) and other related mid-latitude summer nighttime anomaly (MSNA) in the light of international reference ionosphere (IRI)–model," *Adv. Space Res.*, vol. 63, no. 6, pp. 1949–1960, Mar. 2019.
[36] S.-P. Ho, R. A. Anthes, C. O. Ao, S. Healy, A. Horanyi, D. Hunt, A. J. Mannucci, N. Pedatella, W. J. Randel, A. Simmons, A. Steiner, F. Xie, X. Yue, and Z. Zeng, "The COSMIC/FORMOSAT-3 radio occultation mission after 12 years: Accomplishments, remaining challenges, and potential impacts of COSMIC-2," *Bull. Amer. Meteorol. Soc.*, vol. 101, no. 7, pp. E1107–E1136, Jul. 2020.
[37] E. Yiğit and A. S. Medvedev, "Internal gravity waves in the thermosphere during low and high solar activity: Simulation study," *J. Geophys. Res., Space Phys.*, vol. 115, no. A8, pp. n/a–n/a, Aug. 2010.
[38] K.-F. Yang, Y.-H. Chu, C.-L. Su, H.-T. Ko, and C.-Y. Wang, "An examination of FORMOSAT-3/COSMIC ionospheric electron density profile: Data quality criteria and comparisons with the IRI model," *Terr. Atmos. Ocean. Sci.*, vol. 20, pp. 193–206, Oct. 2007.

[39] P. Guo, X. Xu, and G. X. Zhang, "Analysis of the ionospheric equivalent slab thickness based on ground-based GPS/TEC and GPS/COSMIC RO measurements," *J. Atmos. Solar-Terr. Phys.*, vol. 73, nos. 7–8, pp. 839–846, May 2011.
[40] D. Garcia, "Robust smoothing of gridded data in one and higher dimensions with missing values," *Comput. Statist. Data Anal.*, vol. 54, no. 4, pp. 1167–1178, Apr. 2010.
[41] C. H. Lin, C. H. Liu, J. Y. Liu, C. H. Chen, A. G. Burns, and W. Wang, "Midlatitude summer nighttime anomaly of the ionospheric electron density observed by FORMOSAT-3/COSMIC: BRIEF REPORT," *J. Geophys. Res., Space Phys.*, vol. 115, no. A3, Mar. 2010, Art. no. A03308.
[42] R. Penndorf, "The average ionospheric conditions over the antarctic," in *Geomagnetism and Aeronomy: Studies in the Ionosphere, Geomagnetism and Atmospheric Radio Noise*. Washington, DC, USA: AGU, 1965, pp. 1–45.
[43] I. Horvath and E. A. Essex, "The weddell sea anomaly observed with the topex satellite data," *J. Atmos. Solar-Terr. Phys.*, vol. 65, no. 6, pp. 693–706, Apr. 2003.
[44] M. He, L. Liu, W. Wan, B. Ning, B. Zhao, J. Wen, X. Yue, and H. Le, "A study of the weddell sea anomaly observed by FORMOSAT-3/COSMIC: WEDDELL SEA ANOMALY," *J. Geophys. Res., Space Phys.*, vol. 114, no. A12, Dec. 2009, A12309, Art. no. A12309.
[45] R. G. Ezquer, J. L. López, L. A. Scidá, M. A. Cabrera, B. Zolesi, C. Bianchi, M. Pezzopane, E. Zuccheretti, and M. Mosert, "Behaviour of ionospheric magnitudes of f2 region over Tucumán during a deep solar minimum and comparison with the IRI 2012 model predictions," *J. Atmos. Solar-Terr. Phys.*, vol. 107, pp. 89–98, Jan. 2014.
[46] H. Rishbeth and I. C. F. Müller-Wodarg, "Why is there more ionosphere in January than in July? The annual asymmetry in the F2-layer," *Annales Geophysicae*, vol. 24, no. 12, pp. 3293–3311, Dec. 2006.
[47] E. V. Appleton, "Two anomalies in the ionosphere," *Nature*, vol. 157, p. 691, May 1946.
[48] B. G. Fejer, J. W. Jensen, and S.-Y. Su, "Quiet time equatorialFregion vertical plasma drift model derived from ROCSAT-1 observations," *J. Geophys. Res., Space Phys.*, vol. 113, no. A5, May 2008, Art. no. A05304.
[49] S. Tulasi Ram, S.-Y. Su, and C. H. Liu, "FORMOSAT-3/COSMIC observations of seasonal and longitudinal variations of equatorial ionization anomaly and its interhemispheric asymmetry during the solar minimum period," *J. Geophys. Res., Space Phys.*, vol. 114, no. A6, Jun. 2009, Art. no. A06311.
[50] M. R. Torr and D. G. Torr, "The seasonal behaviour of the F2-layer of the ionosphere," *J. Atmos. Terr. Phys.*, vol. 35, no. 12, pp. 2237–2251, Dec. 1973.
[51] H. Rishbeth, "How the thermospheric circulation affects the ionospheric F2-layer," *J. Atmos. Solar-Terr. Phys.*, vol. 60, no. 14, pp. 1385–1402, Sep. 1998.
[52] X. Yue, W. S. Schreiner, J. Lei, S. V. Sokolovskiy, C. Rocken, D. C. Hunt, and Y.-H. Kuo, "Error analysis of abel retrieved electron density profiles from radio occultation measurements," *Annales Geophysicae*, vol. 28, no. 1, pp. 217–222, Jan. 2010.
[53] W. Bai, Y. Sun, J. Xia, G. Tan, C. Cheng, G. Yang, Q. Du, X. Wang, D. Zhao, Y. Tian, X. Zhang, M. Liao, Y. Liu, X. Meng, C. Liu, Y. Cai, and D. Wang, "Validation results of maximum S4 index in F-layer derived from GNOS on FY3C satellite," *GPS Solutions*, vol. 23, no. 1, p. 19, Dec. 2018.
[54] B. S. Potula, Y.-H. Chu, G. Uma, H.-P. Hsia, and K.-H. Wu, "A global comparative study on the ionospheric measurements between COSMIC radio occultation technique and IRI model," *J. Geophys. Res., Space Phys.*, vol. 116, no. A2, Feb. 2011, Art. no. A02310.
[55] H. G. Mayr and K. K. Mahajan, "Seasonal variation in the F2 region," *J. Geophys. Res.*, vol. 76, no. 4, pp. 1017–1027, Feb. 1971.
[56] R. Ma, J. Xu, and H. Liao, "The features and a possible mechanism of semiannual variation in the peak electron density of the low latitude F2 layer," *J. Atmos. Solar-Terr. Phys.*, vol. 65, no. 1, pp. 47–57, Jan. 2003.
[57] Z. Zeng, A. Burns, W. Wang, J. Lei, S. Solomon, S. Syndergaard, L. Qian, and Y.-H. Kuo, "Ionospheric annual asymmetry observed by the COSMIC radio occultation measurements and simulated by the TIEGCM," *J. Geophys. Res., Space Phys.*, vol. 113, no. A7, Jul. 2008, Art. no. A07305.
[58] M. Mendillo, C.-L. Huang, X. Pi, H. Rishbeth, and R. Meier, "The global ionospheric asymmetry in total electron content," *J. Atmos. Sol.-Terr. Phys.*, vol. 67, no. 15, pp. 1377–1387, Sep. 2005.
[59] X. Luan and S. C. Solomon, "Meridional winds derived from COSMIC radio occultation measurements," *J. Geophys. Res., Space Phys.*, vol. 113, no. A8, Aug. 2008, Art. no. A08302.

WEIHUA BAI is currently a Professor with the National Space Science Center, Chinese Academy of Sciences. His current research interests include global navigation satellite system (GNSS) radio occultation and GNSS-R remote sensing techniques. He is also a member of the International GNSS Occultation Working Group (IGOWG) and the China-Europe GNSS-R Remote Sensing Working Group. He served as the Director or the Deputy Director in FY3 series GNOS and GNOSII missions.

GUANGYUAN TAN is currently pursuing the master's degree with the National Space Science Center, Chinese Academy of Sciences. His current research interests include global navigation satellite system (GNSS) radio occultation technology and the improvement of retrieval precision of ionospheric occultation data.

YUEQIANG SUN is currently a Professor with the National Space Science Center, Chinese Academy of Sciences. She devotes to develop global navigation satellite system (GNSS) remote sensing and spaceborne special environment exploration technologies. She has been the principal investigator or vice principal investigator of more than 20 missions/projects in manned space flight, FengYun, and national natural science foundation (863) areas. Her research interests include GNSS radio occultation, GNSS-R remote sensing techniques, atmospheric physics, ionospheric physics, magnetic physics, and space physics.

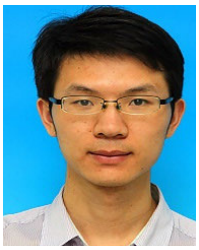

JUNMING XIA is currently pursuing the Ph.D. degree with the National Space Science Center, Chinese Academy of Sciences. His research interests include global navigation satellite system (GNSS) radio occultation and GNSS-R remote sensing techniques.

QIFEI DU is currently pursuing the Ph.D. degree with the National Space Science Center, Chinese Academy of Sciences. His research interest includes space-borne applications of global navigation satellite system (GNSS) signal, including GNSS occultation and GNSS-R remote sensing. His interested technical fields are GNSS receiver, antenna, and microwave circuits development. He has been the principal investigator of the occultation payloads for Yinghuo Satellite and Fengyun-3 Satellites.

GUANGLIN YANG is currently pursuing the Ph.D. degree with the National Space Science Center, Chinese Academy of Sciences. His research interest includes global navigation satellite system (GNSS) meteorological research.

XIANGGUANG MENG is currently pursuing the Ph.D. degree with the National Space Science Center, Chinese Academy of Sciences. His research interests include global navigation satellite system (GNSS) precise orbit determination and radio occultation data processing.

DANYANG ZHAO is currently pursuing the master's degree with the National Space Science Center, Chinese Academy of Sciences. His research interests include data processing of the global navigation satellite system (GNSS) remote sensing and GIS data visualization.

CONGLIANG LIU is currently pursuing the Ph.D. degree with the National Space Science Center, Chinese Academy of Sciences. He currently works on atmosphere and climate monitoring and analysis using radio occultation data. His research interest includes LEO–LEO microwave occultation technique.

YUERONG CAI is currently pursuing the Ph.D. degree with the National Space Science Center, Chinese Academy of Sciences. His research interests include the design of complex high-speed digital circuit system and radiation hardening.

DONGWEI WANG is currently pursuing the Ph.D. degree with the National Space Science Center, Chinese Academy of Sciences. His research interest includes the development and test of the global navigation satellite system (GNSS) radio occultation sounder.

CONG YIN holds a postdoctoral position at the National Space Science Center, Chinese Academy of Sciences. His research interests include global navigation satellite system (GNSS) radio occultation and GNSS-R remote sensing techniques.

PENG HU received the M.Sc. degree from Chang'an University, in 2019. He currently works at the National Space Science Center, Chinese Academy of Sciences. His research interests include GNSS precise orbit determination and the integrated orbit determination of low earth orbit (LEO) and global navigation satellite system (GNSS) satellites.